Sensitivity to Initial and Boundary Perturbations in Convective-Scale Ensemble-Based Data Assimilation: Imperfect-Model OSSEs

Paula Maldonado[1, 2], Juan Ruiz[1, 2], and Celeste Saulo[2, 3]

[1]*Universidad de Buenos Aires - Consejo Nacional de Investigaciones Científicas y Técnicas*, *Centro de Investigaciones del Mar y la Atmósfera (CIMA/UBA-CONICET)*, *Buenos Aires*, *Argentina*

[2]*Universidad de Buenos Aires*, *Facultad de Ciencias Exactas y Naturales*, *Departamento de Ciencias de la Atmósfera y los Océanos (DCAO/FCEN/UBA)*, *Buenos Aires*, *Argentina*

[3]*Consejo Nacional de Investigaciones Científics y Técnicas*, *Servicio Meteorológico Nacional*, *Buenos Aires*, *Argentina*

Abstract

This study investigates the impact of applying different types of initial and boundary perturbations for convective-scale ensemble data assimilation systems. Several observing system simulation experiments (OSSEs) were performed with a 2-km horizontal resolution, considering a realistic environment, taking model error into account, and combining different perturbations' types with warm/cold start initialization. Initial perturbations produce a long-lasting impact on the analysis's quality, particularly for variables not directly linked to radar observations. Warm-started experiments provide the most accurate analysis and forecasts and a more consistent ensemble spread across the different spatial scales. Random small-scale perturbations exhibit similar results, although a longer convergence time is required to up-and-downscale the initial perturbations to obtain a similar error reduction. Adding random large-scale perturbations reduce the error in the first assimilation cycles but produce a slightly detrimental effect afterward.

(**Citation**: Maldonado, P., J. Ruiz, and C. Saulo, 2021: Sensitivity to initial and boundary perturbations in convective-scale ensemble-based data assimilation: imperfect-model OSSEs. *SOLA*, **17**, 96−102, doi:10.2151/sola.2021-015.)

1. Introduction

Over the past decade, much insight has been gained regarding the process of optimally perturbing the initial conditions of convective-scale ensemble prediction systems. Generating multiscale initial conditions perturbations using ensemble-based data assimilation systems (EDAS) has proven to enhance convective-scale forecasts compared to downscaled initial conditions from a coarser-resolution ensemble (Johnson et al. 2014; Johnson and Wang 2016; Raynaud and Bouttier 2016; Surcel et al. 2017). However, the design of initial perturbations for convective-scale EDAS remains a significant challenge, mainly related to the difficulty of recovering all the resolved scales over a regional domain (Gustafsson et al. 2018). Therefore, a multiscale approach is necessary to produce ensemble perturbations that capture the synoptic-scale forcing, the mesoscale phenomena, and the convective scales to be predicted.

Snyder and Zhang (2003) were among the first to address the issue of ensemble initialization in the context of radar data assimilation (RDA). Each ensemble member was initialized by adding Gaussian noise to the velocity field and the liquid-water potential temperature, considering a horizontally homogeneous environment based on a real-sounding. One method applied independent noise at each grid point, and the other localized it to the surroundings of the storm position. The authors found that the choice of the initial ensemble strongly affected the performance of the ensemble Kalman filter (EnKF; Evensen 1994) as the localized noise method reduced the development of spurious convection within the domain. In this direction, Dowell et al. (2004) also localized the initial perturbations to the storm location but added ellipsoidal perturbations to the model fields in a local region of the domain. Smooth random perturbations produced better retrievals and more ensemble spread throughout the assimilation period than a random grid-point noise initialization.

In convective-scale EDAS, the use of regional models requires an appropriate specification of lateral boundary conditions (LBC) perturbations to capture the associated uncertainty and prevent the loss of ensemble variance with increasing time (Nutter et al. 2004; Clark et al. 2008). A mesoscale EDAS could be the optimal method to generate an ensemble of LBC as it provides state-dependent covariances. Many recent studies have used a nested-grid EnKF strategy to account for mesoscale uncertainties through the initial ensemble and LBC perturbations (Stensrud and Gao 2010; Yussouf et al. 2013; Snook et al. 2015; Maejima et al. 2017). However, this method can be computationally expensive. In the absence of a global/mesoscale ensemble, Torn et al. (2006) presented several approaches to generate a LBC ensemble. They assumed different relationships of the LBC spatiotemporal covariances. The results suggest that these methods produce errors that are limited to the lateral boundaries and decay inside the limited-area domain. Moreover, the impact of LBCs uncertainty upon the ensemble spread was studied by Ouaraini et al. (2015) for a mesoscale EDAS. The results indicate that the ensemble spread is sensitive to the amplitude of the LBC perturbations that are randomly drawn from an error covariance model (as suggested by Torn et al. 2006).

This study assesses the sensitivity of a convective-scale radar data assimilation system to different types of initial and boundary conditions (IC-BC) perturbations. Several observing system simulation experiments (OSSEs) of a mesoscale convective system (MCS) case study were conducted with realistic environmental conditions, taking model error into account and using different combinations of perturbations. The sensitivity of the analyses mean and short-range precipitation forecasts to the perturbations' type and amplitude is studied. We focus on the impact of perturbations on ensemble spread and the analysis error at different spatial scales. The rest of the paper is outlined as follows: Section 2 describes the experimental design, section 3 discusses the results, and section 4 summarizes the conclusions.

2. Experimental setting

Based on an OSSE approach, the Weather Research and Forecasting model v3.6 (WRF; Skamarock et al. 2008) is used to gen-

Corresponding author: Paula Maldonado, Centro de Investigaciones del Mar y la Atmósfera (CONICET-UBA), Intendente Güiraldes 2160 (C1428EGA), Buenos Aires, Argentina. E-mail: paula.maldonado@cima.fcen.uba.ar

erate a high-resolution nature run consisting of a long-lived squall line that produced intense surface winds and high-precipitation rates on 22 January 2014. The nature run is integrated between 1200−2200 UTC and consists of a three-nested domain simulation with 10-km, 2-km, and 500-m horizontal grid spacing. The Global Forecast System (GFS; NCEP) operational analysis data with 0.5° horizontal grid spacing and 6-hr frequency is used as IC-BC in the outer domain. The high-resolution nature run domain covers 500 km^2 of the Argentine central region and uses 60 vertical levels. Reflectivity and radial velocity observations are simulated every 5 minutes in radar coordinates considering a radar placed in the center of the high-resolution nature run domain. The radar observation operator of Tong and Xue (2005) is applied to simulate and assimilate the observations, with a Gaussian distributed random observational error with zero mean and standard deviation of 2.5 dBZ for reflectivity and 1 m s^{-1} for radial velocity.

Data assimilation experiments are carried out with the WRF-LETKF system developed by Miyoshi and Kunii (2012) between 1730−2000 UTC and using a 60-member ensemble. The assimilation domain is the same as the 500-m resolution nature run, but a coarser horizontal resolution of 2 km is employed to take model error into account (Maejima et al. 2019). Additionally, IC-BC are taken directly from the GFS model with no downscaling. "No-precipitation" observations, deemed as less than 0 dBZ, are assimilated to prevent the development of spurious convection (Tong and Xue 2005; Aksoy et al. 2009). The configuration of the assimilation system closely follows the one used in Maldonado et al. (2020). Supplement 1 provides detailed information about the model domain and the WRF-LETKF system configuration.

The initial background ensemble is generated at 1730 UTC using a cold-start (CS) or a warm-start (WS) approach. For both, ensemble members are created by adding random perturbations to the GFS analysis data. The WS approach considers the spin-up time of moist processes through a free forecast ran 5.5-hr before the initial time of RDA experiments (spin-up model run hereafter). It allows small-scale perturbations to develop throughout the domain as the model can generate an MCS by 1730 UTC. The LBC ensemble is provided every 5 minutes and is obtained by adding random perturbations to the GFS analysis data.

Two classes of random perturbations are employed to represent the multiscale nature of IC-BC uncertainty. On the one hand, small-scale perturbations (SS) are added to the wind, temperature, and relative humidity fields within the assimilation domain, sampling them from a Gaussian distribution with zero mean and standard deviation of 0.25 m s^{-1}, 0.25 K, and 2.5 g kg^{-1}, respectively. Previous assimilation experiments using a larger amplitude showed detrimental results as spurious convection developed in the analysis, significantly modifying the MCS environment. The SS perturbations are smoothed spatially by applying a two-dimensional Lanczos filter (Duchon 1979) in the horizontal direction followed by a vertical one-dimensional filter. The chosen horizontal and vertical length-scales are 40 km and ~ 5 km, respectively, similar to the correlation scales of the simulated mode of convection organization (Dowell and Wicker 2009).

On the other hand, large-scale perturbations (LS) are generated as scaled differences between two random atmospheric states with a smooth time evolution as in Necker et al. (2020). In this way, we preserved the nearly hydrostatic and geostrophic equilibrium of larger scales. A large sample of atmospheric states of size $N = 5840$ is obtained from the Climate Forecast System Reanalysis (CFSR) data between 2006−2009, with 6-h time-frequency (Δt) and 0.5° horizontal grid spacing. In the first assimilation cycle at time $t = t_s$, the i-th perturbation is computed as:

$$X'^{i}_{LS}(t_s) = \alpha_{LS}[X(t_1) - X(t_2)]$$

where α_{LS} is the amplitude scaling factor, $X(t_1)$ and $X(t_2)$ are the CFSR analysis states at times $t_1 = n^i_1 \Delta t$ and $t_2 = n^i_2 \Delta t$, respectively, with $n^i_{1,2} \in [0; N]$ randomly chosen and only restricted to t_1 and t_2 corresponding to the same time of the year. In the following assimilation cycles at time $t > t_s$, the i-th perturbation is computed as:

Table 1. List of assimilation experiments describing the initialization approach, the use of small-scale (SS) perturbations, and the large-scale (LS) perturbations amplitude scaling factor α_{LS}.

Experiment name	Initialization	SS perturbation	LS perturbation
CS-LS5%	Cold-start	No	$\alpha_{LS} = 0.05$
CS-LS10%	Cold-start	No	$\alpha_{LS} = 0.1$
SSCS	Cold-start	Yes	$\alpha_{LS} = 0$
SSCS-LS5%	Cold-start	Yes	$\alpha_{LS} = 0.05$
SSCS-LS10%	Cold-start	Yes	$\alpha_{LS} = 0.1$
SSWS	Warm-start	Yes	$\alpha_{LS} = 0$
SSWS-LS5%	Warm-start	Yes	$\alpha_{LS} = 0.05$

$$X'^{i}_{LS}(t) = \alpha_{LS}[(1-\beta)*(X(t^i_{l1}) - X(t^i_{l2})) + \beta*(X(t^i_{u1}) - X(t^i_{u2}))]$$

where $t^i_{l1,2} = (n^i_{1,2} + n)\Delta t$ and $t^i_{u1,2} = (n^i_{1,2} + n + 1)\Delta t$, with $n = \text{floor}[(t - t_s)/\Delta t]$, and $\beta = \delta/\Delta t$ is a linear interpolation time factor to compute perturbations at arbitrary times (not necessarily a multiple of Δt), with $\delta = t_s - n\Delta t$.

Seven assimilation experiments are performed combining warm/cold initialization with a given type and amplitude of the perturbations to generate the IC-BC ensembles (Table 1). CS-LS5% and CS-LS10% are cold-started using only large-scale perturbations with a different amplitude scaling factor. SSCS, SSCS-LS5%, and SSCS-LS10% are cold-started using small-scale perturbations with increasing LS amplitude scaling factor, being zero for SSCS. Similarly, SSWS and SSWS-LS5% include small-scale perturbations, but only SSWS-LS5% includes large-scale perturbations, and both are warm-started with the spin-up model run using the corresponding random perturbations.

For each experiment, 2-hr ensemble forecasts are initialized at 1830 UTC, 1900 UTC, and 1930 UTC from the corresponding 60-member analysis ensemble. The forecast LBC ensemble uses the same random perturbations as in the corresponding assimilation experiment. A free model run with no assimilation of observations (NoDA) is performed for comparison. NoDA is a warm-started deterministic forecast initialized at 1730 UTC from the mean of the 60-member ensemble taken from the same spin-up model run used in SSWS-LS5%. Verification metrics to assess the performance of both analysis and forecasts are computed using a smoothed version of the high-resolution nature run (i.e., applying a box-averaging interpolation technique to match the assimilation experiment's resolution).

3. Results and discussion

An example of the impact of RDA on short-range forecasts is given by comparing NoDA and SSWS-LS5% against the nature run. Figure 1 shows the time evolution of 30-min accumulated precipitation and 30-min maximum 10-m wind fields of the forecast initialized at 1830 UTC, as the analysis could correctly retrieve the squall line structure from that time onward (not shown). Forecast lead times of 30, 60, and 90 minutes (i.e., valid at 1900 UTC, 1930 UTC, and 2000 UTC) are shown. SSWS-LS5% can accurately retrieve the location, intensity, and extension of the squall line up to a 90-min lead time. Even though NoDA can forecast a convective system similar to that in the nature run, the MCS location and timing are not as accurate as in SSWS-LS5%, and some isolated spurious cells developed west of the squall line. Therefore, when the forecast's initial condition contains information on the mesoscale (through RDA), it becomes more skillful.

The sensitivity to the perturbations applied to generate the ensemble is assessed through grid point metrics. Space-averaged root-mean-square error (RMSE) and ensemble spread (SPREAD) are computed over grid points where reflectivity is greater than 0 dBZ either in the analysis ensemble mean or in the nature run. Figure 2 shows, the RMSE and SPREAD of zonal wind, temperature, and ref-condensates (defined as the sum of rain, snow, and

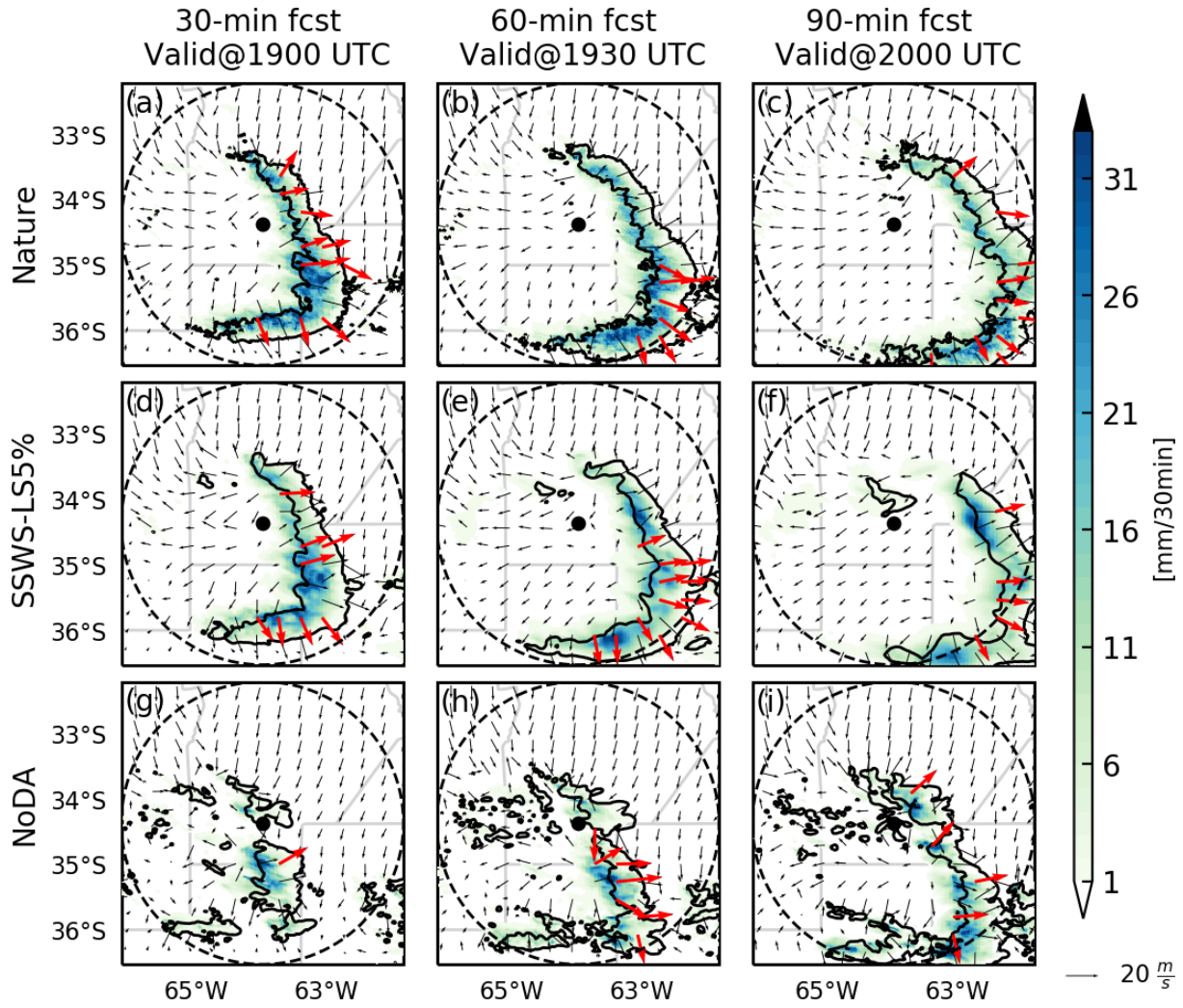

Fig. 1. Time evolution of 30-min accumulated precipitation field (shaded) and 30-min maximum 10-m wind field (vectors; m s^{-1}) of the ensemble forecast initialized at 1830 UTC, with forecast lead times of 30, 60, and 90 minutes. The 10 dBZ contour (black line) outlines the edge of the squall line and red arrows indicate wind magnitude larger than 17 m s^{-1}. Radar maximum range (dashed black line) and location (black dot) are shown for reference. (a)−(c) Nature run, (d)−(f) SSWS-LS5% forecast ensemble mean, and (g)−(i) NoDA deterministic forecast.

graupel mixing ratios as these species are involved in the reflectivity computation). All variables RMSE is considerably reduced during the first assimilation hour, and afterward, it stabilizes for all experiments, suggesting a filter spin-up period from 1730−1830 UTC.

Warm-started experiments outperform cold-started ones as they exhibit higher SPREAD and lower RMSE during the first assimilation hour. Moreover, CS experiments approach a similar SPREAD value as in WS experiments after roughly 30, 75, and 100 minutes for temperature, zonal wind, and ref-condensates, respectively. The initial SPREAD of SSCS, CS-LS5%, and SSCS-LS5% is very similar. However, the growth rate during the filter spin-up is quite different, ultimately impacting the analysis error. For instance, CS-LS5% shows the slowest growth rate during the filter spin-up and the largest mean error after that period. The most substantial impact of initial perturbations is observed in temperature, presenting large RMSE differences between experiments, even though the SPREAD differences are not so notorious. Up to 60 minutes, SSCS-LS5% and SSCS-LS10% RMSE are lower than SSCS. Afterward, this effect is reversed, suggesting that applying LS perturbations helps the filter converge faster to the nature run but slightly degrades the analysis once it reaches convergence. Additionally, all experiments are under-dispersive after the filter spin-up, even when using optimal inflation and localization parameters (Maldonado et al. 2020).

To investigate how different perturbations impact the ensemble spread within convective areas and their environment, Fig. 3 presents the ensemble spread evolution in convective and non-convective regions, defined as grid points where reflectivity is greater than 0 dBZ and less than −10 dBZ, respectively. Large-scale perturbations allow maintaining a high SPREAD throughout the assimilation in non-convective areas and after the filter spin-up inside convective cells. However, this does not have a positive impact on the analysis skill as the ensemble is under-dispersive. Additionally, the perturbations' structure impacts the initial convergence as it modulates the SPREAD growth rate during the first few cycles. For instance, SPREAD increases more rapidly in convective regions when a larger amplitude of the LS perturbations or when both SS and LS perturbations are applied. Figure 4 illustrates the impact of initial perturbations during the filter spin-up (at 1750 UTC) upon the assimilation of radar observations. The developing convective system is better retrieved by WS experiments and by CS experiments using LS and SS perturbations. However, the MCS representation is quite different in experiments with a similar initial SPREAD (e.g., SSCS and CS-LS5%), suggesting that the perturbations' structure rather than its magnitude mostly control the process of convection initiation.

The influence of the perturbation type on different spatial

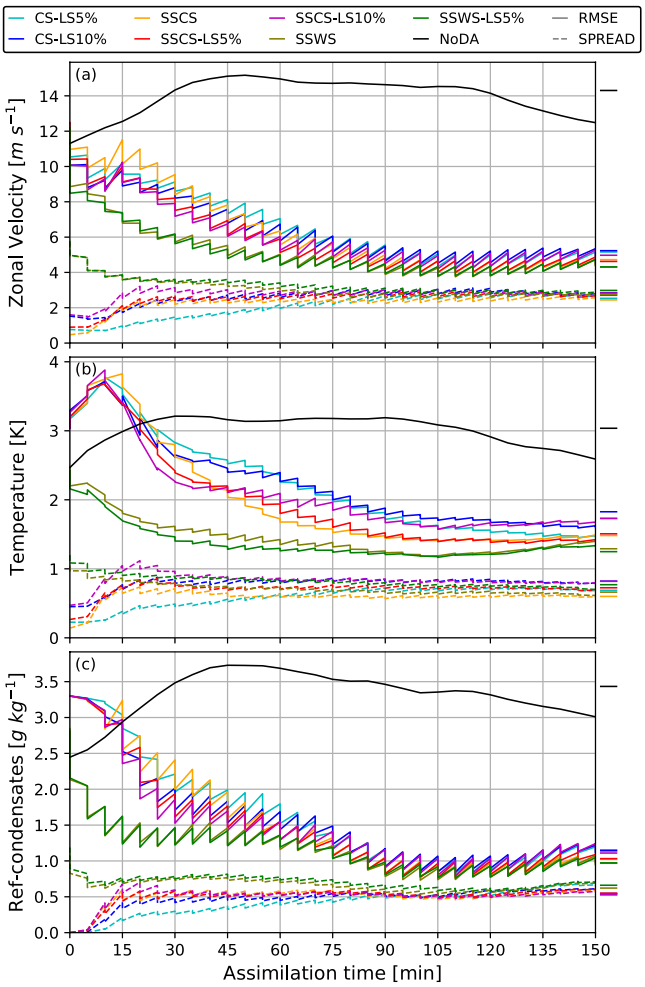

Fig. 2. Time evolution of the space-averaged analysis mean RMSE (solid line) and SPREAD (dashed line) for CS-LS5% (cyan line), CS-LS10% (blue line), SSCS (yellow line), SSCS-LS5% (red line), SSCS-LS10% (purple line), SSWS (olive line), and SSWS-LS5% (green line). NoDA RMSE (black line) is shown for reference. Scores average include grid points where reflectivity is greater than 0 dBZ either in the assimilation experiment or in the nature run. The horizontal line next to the graph indicates the time mean between 60−150 min of assimilation time. (a) Zonal wind, (b) temperature, and (c) ref-condensates.

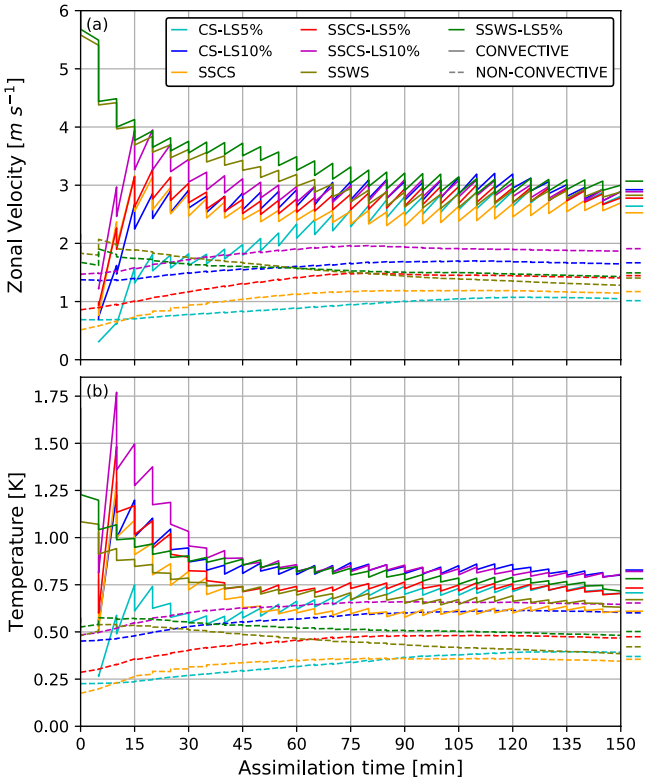

Fig. 3. Time evolution of the space-averaged analysis ensemble spread in convective (solid line) and non-convective (dashed line) regions, for CS-LS5% (cyan line), CS-LS10% (blue line), SSCS (yellow line), SSCS-LS5% (red line), SSCS-LS10% (purple line), SSWS (olive line), and SSWS-LS5% (green line). Convective and non-convective regions are defined as grid points where reflectivity is greater than 0 dBZ, and less than −10 dBZ, respectively. (a) Zonal wind, and (b) temperature.

scales is investigated by performing a spectral decomposition of the squared analysis ensemble perturbations (SAEP), defined as the square difference between an ensemble member and the ensemble mean. A discrete Fourier transform is applied to the SAEP longitudinal series followed by a latitudinal average to obtain a one-dimensional spectrum for each ensemble member. Finally, the SAEP mean spectrum is obtained by averaging over all ensemble members. Figure 5 shows the 8-km zonal wind SAEP mean spectrum and ensemble mean square error spectra, for CS-LS10%, SSCS, and SSWS. At this height, the spatial scales the analysis can correctly capture extend up to 6 km wavelength (Maldonado et al. 2020).

CS-LS10% initial spectrum concentrates the energy at wavelengths larger than 100 km. An energy cascade from large to small scales is observed once the assimilation starts, taking approximately 20−40 minutes to significantly increase the spectral energy for wavelengths close to 10 km. For SSCS, the initial spectrum concentrates the energy for wavelengths longer than 40 km. Once the spectrum starts to evolve under the system dynamics, energy increases both upscale and downscale from the perturbation's characteristic length of 40 km. The downscale process takes more time than the upscale one, taking approximately 30−50 minutes to develop small-scale structures. Lastly, SSWS initial spectrum distributes the energy throughout the different spatial scales with a maximum in the large-scale part of the spectrum, and the energy decreases with assimilation time.

Compared to the analysis mean square error spectrum (Figs. 5b, 5d, and 5f), all experiments underestimate the spectral energy intensity at the mesoscale, consistent with the ensemble being under-dispersive (cf. Fig. 2). CS-LS10% keeps a high ensemble variance throughout the assimilation time but lacks enough variance at small-scales at the beginning of the cycle. The error spectrum's time-frequency variability is better represented by SSWS (especially at the initial time), allowing for a more consistent reduction of the analysis error at scales below 100 km, where radar data most effectively constrain the model solution.

Finally, a spatial verification of short-range precipitation forecasts is assessed by using a probabilistic version of the fraction skill score (FSS; Roberts and Lean 2008) in which the forecast probability is used instead of the ensemble forecast mean. Figure 6 shows the FSS of 30-min accumulated precipitation for 1-mm and 15-mm threshold, as a function of spatial scale and forecast lead time. For a 1 mm threshold, CS-LS5%, CS-LS10%, and SSCS-LS10% exhibit a lower FSS than the rest of the experiments for spatial scales smaller than 100 km and forecast lead times longer than 50 minutes. For a 15-mm threshold, the sensitivity to the type of perturbations is more significant both as a function of spatial scales and forecast lead times. In particular, experiments using the largest amplitude of large-scale perturbations exhibit the lowest FSS, while SSWS shows the highest score. Moreover, including LS perturbations in WS experiments slightly seems to degrade the forecast.

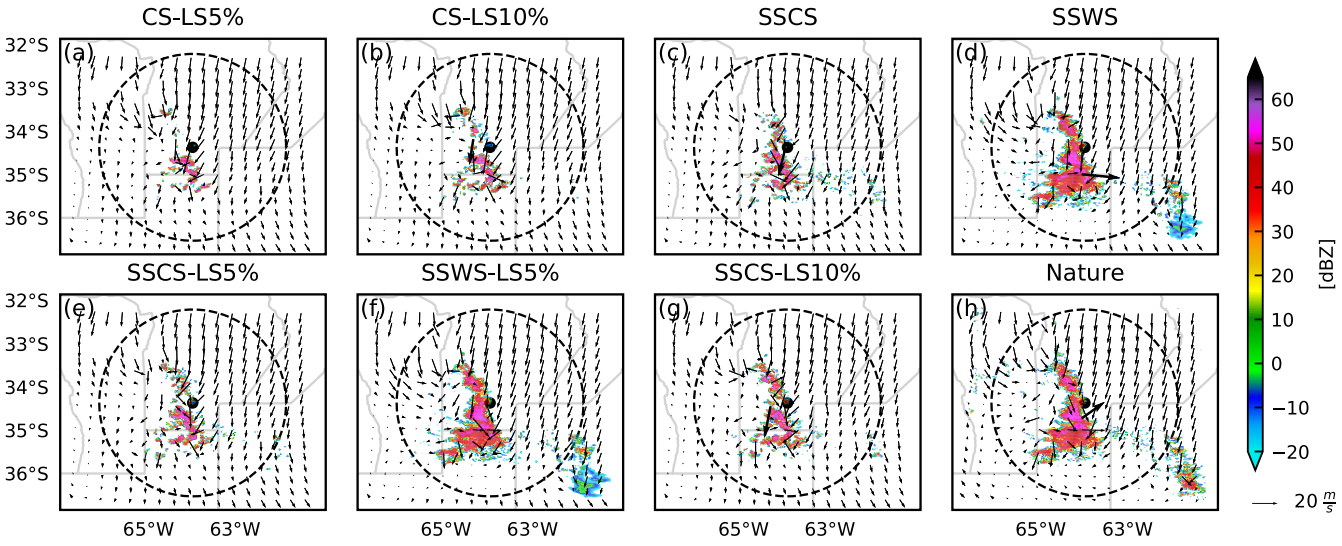

Fig. 4. Analysis mean reflectivity field (shaded) and horizontal wind field (vectors; m s^{-1}) at z = 1 km and 1750 UTC. Thick arrows indicate wind magnitude larger than 20 m s^{-1}. Radar maximum range (dashed black line) and location (black dot) are shown for reference. (a) CS-LS5%, (b) CS-LS10%, (c) SSCS, (d) SSWS, (e) SSCS-LS5%, (f) SSWS-LS5%, (g) SSCS-LS10%, and (h) Nature run.

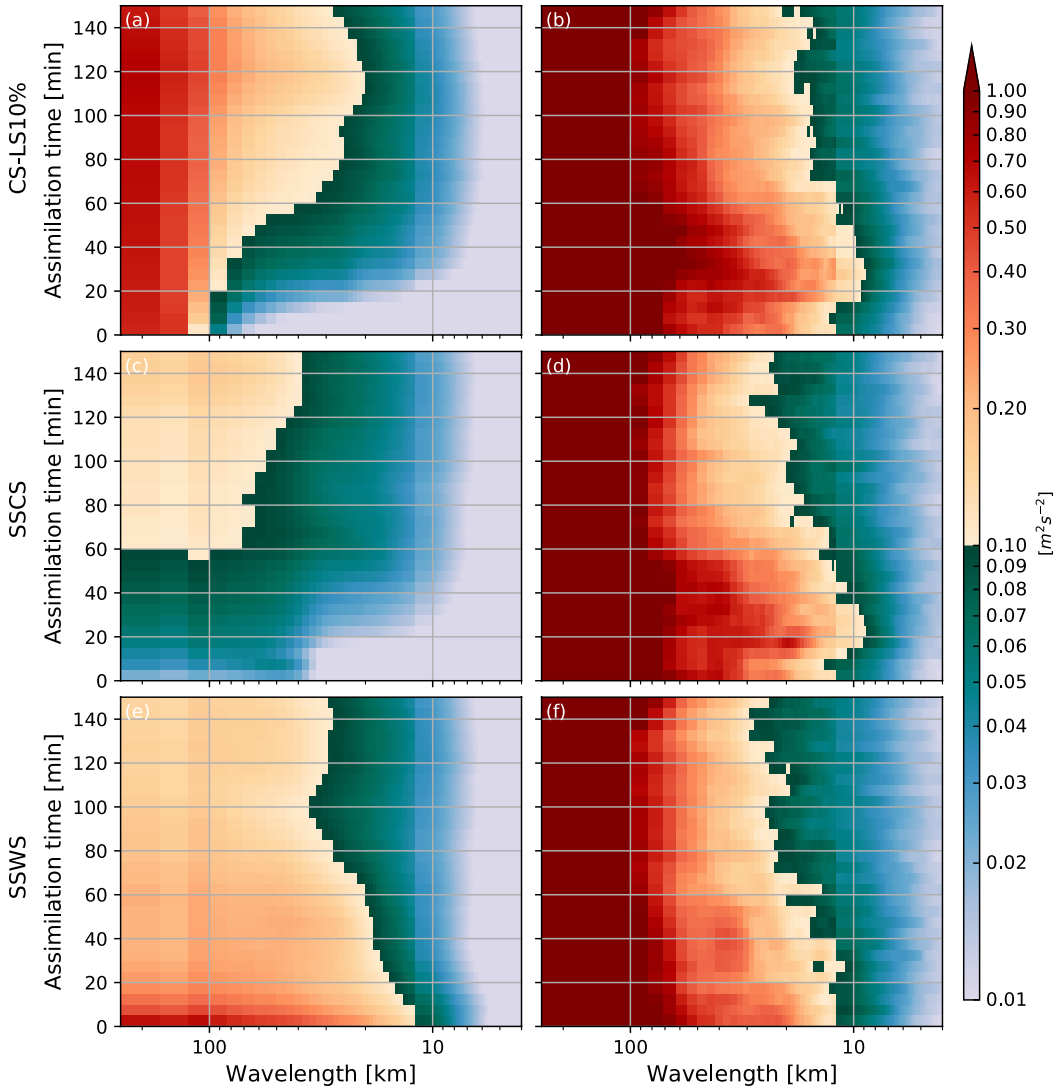

Fig. 5. Time evolution of the squared analysis ensemble perturbations (SAEP) mean spectrum and analysis ensemble mean square error spectra of zonal velocity at z = 8 km. (a)−(b) CS-LS10%, (c)−(d) SSCS, and (e)−(f) SSWS.

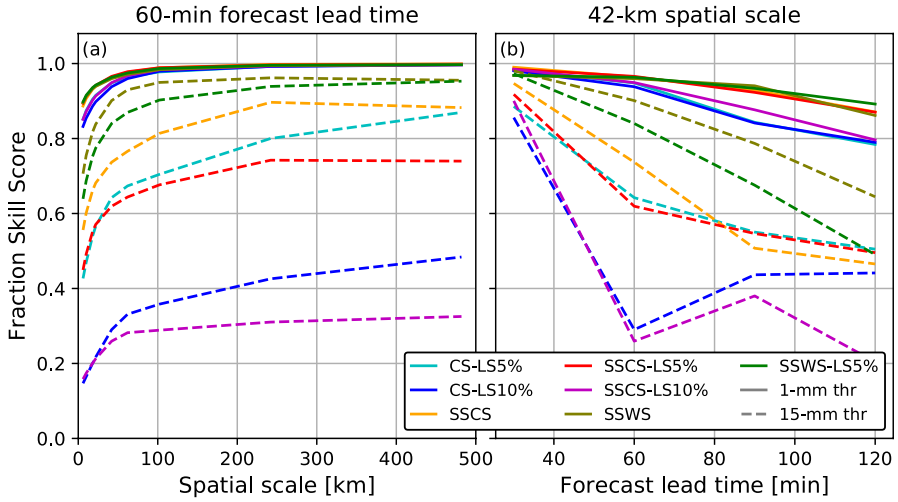

Fig. 6. 30-min accumulated precipitation fraction skill score (FSS) for 1-mm (solid line) and 15-mm (dashed line) thresholds, for CS-LS5% (cyan line), CS-LS10% (blue line), SSCS (yellow line), SSCS-LS5% (red line), SSCS-LS10% (purple line), SSWS (olive line), and SSWS-LS5% (green line). (a) FSS as a function of spatial scale for a 60-min forecast lead time, and (b) FSS as a function of forecast lead time for a 42-km spatial scale.

4. Summary

Seven OSSEs were performed to study the impact of applying different IC-BC perturbation types on the WRF-LETKF RDA system. The amplitude and type of IC-BC perturbations have a long-lasting impact on the analysis and forecast quality.

Warm-started experiments produce the best results probably because they provide a consistent distribution of ensemble spread across different spatial scales at the initial time. Random small-scale perturbations yield consistent results, but the time required to downscale and upscale the initial perturbations degrades the analysis quality (particularly during the first hour). Large-scale perturbations lead to even larger filter spin-up since more time is required for the spread to grow at small-scales where radar data more effectively constrains the model solution. Combined with SS perturbations, LS cooperates to maintain the ensemble spread outside the convective system and reduce the error during the first assimilation cycles. However, their long-term impact is slightly detrimental to both the analysis and forecast quality for this MCS system. As mentioned by Torn et al. (2006), the technique described in this paper to generate large-scale perturbations is not optimal, and a regional mesoscale analysis ensemble could be employed to produce dynamically consistent large-scale perturbations.

All experiments resulted in an under-dispersive ensemble. As mentioned by Dowell and Wicker (2009), using additive inflation perturbations could alleviate this problem. Therefore, it might be useful to conduct experiments to evaluate the impact of different perturbation types in that context.

Acknowledgments

The present work was supported by Agencia Nacional de Promoción Científica y Tecnológica (Argentina) Grants PICT 2014-1000 and PICT 2017-2233, Consejo Nacional de Investigaciones Científicas y Técnicas (Argentina) and Universidad de Buenos Aires (Argentina).

Edited by: S.-H. Chen

Supplements

Supplement 1 provides information about the model and methodology.

References

Aksoy, A., D. C. Dowell, and C. Snyder, 2009: A multicase comparative assessment of the ensemble Kalman filter for assimilation of radar observations. Part I: Storm-scale analyses. *Mon. Wea. Rev.*, **137**, 1805−1824, doi:10.1175/2008MWR2691.1.

Clark, A. J., J. Gallus,William A., and T.-C. Chen, 2008: Contributions of mixed physics versus perturbed initial/lateral boundary conditions to ensemble-based precipitation forecast skill. *Mon. Wea. Rev.*, **136**, 2140−2156, doi:10.1175/2007MWR2029.1.

Dowell, D. C., and L. J. Wicker, 2009: Additive noise for storm-scale ensemble data assimilation. *J. Atmos. Oceanic Technol.*, **26**, 911−927, doi:10.1175/2008JTECHA1156.1.

Dowell, D. C., F. Zhang, L. J. Wicker, C. Snyder, and N. A. Crook, 2004: Wind and temperature retrievals in the 17 May 1981 Arcadia, Oklahoma, supercell: Ensemble Kalman filter experiments. *Mon. Wea. Rev.*, **132**, 1982−2005, doi:10.1175/1520-0493(2004)132<1982:WATRIT>2.0.CO;2.

Duchon, C. E., 1979: Lanczos filtering in one and two dimensions. *J. Appl. Meteor.*, **18**, 1016−1022, doi:10.1175/1520-0450(1979)018<1016:LFIOAT>2.0.CO;2.

Dudhia, J., 1989: Numerical study of convection observed during the winter monsoon experiment using a mesoscale two-dimensional model. *J. Atmos. Sci.*, **46**, 3077−3107, doi:10.1175/1520-0469(1989)046<3077:NSOCOD>2.0.CO;2.

Evensen, G., 1994: Sequential data assimilation with a nonlinear quasi-geostrophic model using monte carlo methods to forecast error statistics. *J. Geophys. Res.*, **99**, 10143−10162, doi:10.1029/94JC00572.

Gustafsson, N., and co-authors, 2018: Survey of data assimilation methods for convective-scale numerical weather prediction at operational centres. *Quart. J. Roy. Meteor. Soc.*, **144**, 1218−1256, doi:10.1002/qj.3179.

Hong, S.-Y., and J.-O. J. Lim, 2006: TheWRF single-moment 6-class microphysics scheme (WSM6). *J. Korean Meteor. Soc.*, **42**, 129−151.

Hong, S.-Y., Y. Noh, and J. Dudhia, 2006: A new vertical diffusion package with an explicit treatment of entrainment processes. *Mon. Wea. Rev.*, **134**, 2318−2341, doi:10.1175/MWR3199.1.

Johnson, A., and X. Wang, 2016: A study of multiscale initial condition perturbation methods for convection-permitting ensemble forecasts. *Mon. Wea. Rev.*, **144**, 2579−2604, doi:10.1175/MWR-D-16-0056.1.

Johnson, A., and co-authors, 2014: Multiscale characteristics and

evolution of perturbations for warm season convection-allowing precipitation forecasts: Dependence on background flow and method of perturbation. *Mon. Wea. Rev.*, **142**, 1053−1073, doi:10.1175/MWR-D-13-00204.1.

Lange, H., and G. C. Craig, 2014: The impact of data assimilation length scales on analysis and prediction of convective storms. *Mon. Wea. Rev.*, **142**, 3781−3808, doi:10.1175/MWR-D-13-00304.1.

Maejima, Y., M. Kunii, and T. Miyoshi, 2017: 30-second-update 100-m-mesh data assimilation experiments: A sudden local rain case in kobe on 11 september 2014. *SOLA*, **13**, 174−180, doi:10.2151/sola.2017-032.

Maejima, Y., T. Miyoshi, M. Kunii, H. Seko, and K. Sato, 2019: Impact of dense and frequent surface observations on 1-minute-update severe rainstorm prediction: A simulation study. *J. Meteor. Soc. Japan. Ser. II*, **97**, 253−273, doi:10.2151/jmsj.2019-014.

Maldonado, P., J. Ruiz, and C. Saulo, 2020: Parameter sensitivity of the WRF–LETKF system for assimilation of radar observations: Imperfect-model observing system simulation experiments. *Wea. Forecasting*, **35**, 1345−1362, doi:10.1175/WAF-D-19-0161.1.

Miyoshi, T., and M. Kunii, 2012: The local ensemble transform Kalman filter with the Weather Research and Forecasting model: Experiments with real observations. *Pure and Applied Geophysics*, **169**, 321−333, doi:10.1007/s00024-011-0373-4.

Mlawer, E. J., S. J. Taubman, P. D. Brown, M. J. Iacono, and S. A. Clough, 1997: Radiative transfer for inhomogeneous atmospheres: RRTM, a validated correlated-k model for the longwave. *J. Geophys. Res.*, **102**, 16663−16682, doi:10.1029/97JD00237.

Necker, T., S. Geiss, M. Weissmann, J. Ruiz, T. Miyoshi, and G.-Y. Lien, 2020: A convective-scale 1,000-member ensemble simulation and potential applications. *Quart. J. Roy. Meteor. Soc.*, doi:10.1002/qj.3744.

Nutter, P., D. Stensrud, and M. Xue, 2004: Effects of coarsely resolved and temporally interpolated lateral boundary conditions on the dispersion of limited-area ensemble forecasts. *Mon. Wea. Rev.*, **132**, 2358−2377, doi:10.1175/1520-0493(2004)132<2358:EOCRAT>2.0.CO;2.

Ouaraini, R. E., L. Berre, C. Fischer, and E. H. Sayouty, 2015: Sensitivity of regional ensemble data assimilation spread to perturbations of lateral boundary conditions. *Tellus A*, **67**, doi:10.3402/tellusa.v67.28502.

Raynaud, L., and F. Bouttier, 2016: Comparison of initial perturbation methods for ensemble prediction at convective scale. *Quart. J. Roy. Meteor. Soc.*, **142**, 854−866, doi:10.1002/qj.2686.

Roberts, N. M., and H. W. Lean, 2008: Scale-selective verification of rainfall accumulations from high-resolution forecasts of convective events. *Mon. Wea. Rev.*, **136**, 78−97, doi:10.1175/2007MWR2123.1.

Skamarock, W., and co-authors, 2008: A description of the advanced research WRF version 3. Tech. Rep. NCAR/TN-475+STR, NCAR, 113 pp.

Snook, N., M. Xue, and Y. Jung, 2015: Multiscale EnKF assimilation of radar and conventional observations and ensemble forecasting for a tornadic mesoscale convective system. *Mon. Wea. Rev.*, **143**, 1035−1057, doi:10.1175/MWR-D-13-00262.1.

Snyder, C., and F. Zhang, 2003: Assimilation of simulated Doppler radar observations with an ensemble Kalman filter. *Mon. Wea. Rev.*, **131**, 1663−1677, doi:10.1175/2555.1.

Sobash, R. A., and D. J. Stensrud, 2013: The impact of covariance localization for radar data on EnKF analyses of a developing MCS: Observing system simulation experiments. *Mon. Wea. Rev.*, **141**, 3691−3709, doi:10.1175/MWR-D-12-00203.1.

Stensrud, D. J., and J. Gao, 2010: Importance of horizontally inhomogeneous environmental initial conditions to ensemble storm-scale radar data assimilation and very short-range forecasts. *Mon. Wea. Rev.*, **138**, 1250−1272, doi:10.1175/2009MWR3027.1.

Surcel, M., I. Zawadzki, M. K. Yau, M. Xue, and F. Kong, 2017: More on the scale dependence of the predictability of precipitation patterns: Extension to the 2009−13 CAPS spring experiment ensemble forecasts. *Mon. Wea. Rev.*, **145**, 3625−3646, doi:10.1175/MWR-D-16-0362.1.

Tewari, M., and co-authors, 2004: Implementation and verification of the united noah land surface model in the wrf model. *20th Conf. on Weather Analysis and Forecasting/16th Conf. on Numerical Weather Prediction*, 11−15.

Tong, M., and M. Xue, 2005: Ensemble Kalman filter assimilation of Doppler radar data with a compressible nonhydrostatic model: OSS experiments. *Mon. Wea. Rev.*, **133**, 1789−1807, doi:10.1175/MWR2898.1.

Torn, R. D., G. J. Hakim, and C. Snyder, 2006: Boundary conditions for limited-area ensemble Kalman filters. *Mon. Wea. Rev.*, **134**, 2490−2502, doi:10.1175/MWR3187.1.

Weng, Y., and F. Zhang, 2012: Assimilating airborne doppler radar observations with an ensemble Kalman filter for convection-permitting hurricane initialization and prediction: Katrina (2005). *Mon. Wea. Rev.*, **140**, 841−859, doi:10.1175/2011MWR3602.1.

Yussouf, N., E. R. Mansell, L. J. Wicker, D. M. Wheatley, and D. J. Stensrud, 2013: The ensemble Kalman filter analyses and forecasts of the 8 May 2003 Oklahoma City tornadic supercell storm using single- and double-moment microphysics schemes. *Mon. Wea. Rev.*, **141**, 3388−3412, doi:10.1175/MWR-D-12-00237.1.

Manuscript received 14 January 2021, accepted 27 March 2021
SOLA: *https://www.jstage.jst.go.jp/browse/sola/*